ELSEVIER

Using X-ray computed tomography in hydrology: systems, resolutions, and limitations

D. Wildenschild[a,b,*], J.W. Hopmans[c], C.M.P Vaz[d], M.L. Rivers[e], D. Rikard[f], B.S.B. Christensen[a]

[a]*Environment and Resources, Technical University of Denmark, 2800 Lyngby, Denmark*
[b]*Experimental Geophysics Group, Earth and Environmental Sciences Directorate, Lawrence Livermore National Laboratory, Livermore, CA 94551, USA*
[c]*Hydrology, Department of Land, Air and Water Resources, University of California, Davis, CA 95616, USA*
[d]*Embrapa Agricultural Instrumentation, CNPDIA, 13560-970, São Carlos, SP Cx. P. 741, Brazil*
[e]*Consortium for Advanced Radiation Sources and Department of Geophysical Sciences, University of Chicago, Chicago, IL, USA*
[f]*Nondestructive Evaluation Section, Lawrence Livermore National Laboratory, Livermore, CA 94551, USA*

Abstract

A combination of advances in experimental techniques and mathematical analysis has made it possible to characterize phase distribution and pore geometry in porous media using non-destructive X-ray computed tomography (CT). We present qualitative and quantitative CT results for partially saturated media, obtained with different scanning systems and sample sizes, to illustrate advantages and limitations of these various systems, including topics of spatial resolution and contrast. In addition, we present examples of our most recent three-dimensional high-resolution images, for which it was possible to resolve individual pores and to delineate air–water interfacial contacts. This kind of resolution provides a novel opportunity to follow the dynamic flow behavior on the pore scale and to verify new theoretical and numerical modeling approaches. © 2002 Elsevier Science Ltd. All rights reserved.

Keywords: Porous media; Multi-phase flow; X-ray tomography; Synchrotron radiation; Pore structure; Visualization

1. Introduction

A common problem limiting our understanding of multi-phase flow and transport is the lack of information about the microscopic geometry and associated processes in porous media. Recent advances in pore-scale modeling such as network modeling (Celia et al., 1995), and Lattice–Boltzmann modeling (Ferreol and Rothman, 1995) has allowed simulation of fluid flow processes on the micro-scale. On the macro-scale, macro-pore and preferential flow are suggested as important mechanisms for accelerated breakthrough of contaminants, however, to fully understand the significance of immobile water regions, as well as dispersion and diffusion processes, it is becoming increasingly clear that pore-scale measurements are needed. The mechanisms, operating at both macro- and micro-scales, are difficult to understand based on traditional measurement techniques, which generally require insertion of a sensor

at or near the region of interest. Herein, we report on recent investigations using X-ray computed tomography (CT), which is a technique for determining the internal structure of an object. In a conventional two-dimensional shadow radiograph the depth information is lost, but when X-ray transmission information is obtained from a multitude of radiographic images, scanned at different angles, a complete three-dimensional image can be obtained. Over the years, the applications of CT have evolved to cover characterization of specimen pore space with respect to variables such as soil bulk density (Petrovic et al. 1982; Anderson et al., 1990), volumetric water content (Hopmans et al., 1992), spatial correlation, connectivity, and tortuosity (Coles et al., 1998), porosity, pore-volume-to-surface-ratio, permeability, electrical resistivity, and wetting phase residual saturation (Auzerais et al., 1996), and breakthrough of solutes in porous media (Vinegar and Wellington, 1987; Clausnitzer and Hopmans, 2000). Among the most recent applications is the use of CT to describe the physically complex pore space as used in network and pore-scale simulation models (Hazlett, 1995; Ferréol and Rothman, 1995). In very recent work, Held and Celia (2001) used network modeling to support the thermodynamic relationships for multiphase flow developed by Hassanizadeh and Gray (1993). These functional relationships incorporate non-traditional porous media variables such as interfacial areas and common lines, the latter being the contact points between the three phases (solid, air and liquid). Held and Celia (2001) specifically call for measurement techniques capable of resolving these variables. The ability to quantify phase interfaces and common lines in a non-destructive way will make it possible to evaluate recent theoretical and numerical model developments, particularly, Lattice–Boltzmann models that rely on detailed information about the geometry of the porous medium. Currently, this information cannot be obtained with existing indirect measurement techniques.

In this paper, we compare results obtained with three different CT systems: An industrial X-ray tube with a spatial resolution of 400 µm, a medical scanner with a resolution of 100–500 µm, and a synchrotron-based computed micro-tomography (CMT) system providing a spatial resolution of 5–20 µm. Using these three X-ray systems, we have obtained images of spatial distribution of the solid, liquid and gaseous phases over a range of spatial scales and with different spatial resolutions. Depending on the type of measurement system, the reconstructed images provide information on macroscopic saturation profiles or detailed microscopic pore geometry information, including interfacial area and curvature. We discuss limitations and error sources, spatial resolution, and contrast sensitivity. The overall objective of the study is to provide guidelines for hydrologists in selecting X-ray CT measurement system, sample size, and use of a chemical additive (dopant), in accordance with the targeted research application.

2. X-ray tomography fundamentals

Conventional X-rays are produced in a highly evacuated glass bulb of an X-ray tube, consisting of two electrodes: usually a platinum or tungsten (high atomic weight material) anode and a cathode. When a high voltage is applied between these electrodes, accelerated electrons (cathode rays) produce X-rays (electromagnetic radiation) as they strike the anode. Two different processes produce radiation in the X-ray frequency range from 10^{16} to 10^{21} Hz, corresponding to wavelengths of 10^{-8}–10^{-11} cm and photon energies from 200 to 100.000 eV. First, the high-speed electrons themselves produce radiation as they are decelerated by the positively charged nuclei of the anode material. This radiation is defined as bremsstrahlung (German for braking radiation). Second, X-ray radiation is emitted when excited electrons of the anode material fall back to a lower-energy shell position from a higher energy state, after first having been knocked out of their K-shell position by the incoming high-speed electrons. The resulting sharp peaks are characteristic of the X-ray line spectrum for the anode material and will differ between anode materials. The two processes combined result in a broad continuous spectrum of frequencies to yield a polychromatic beam. Commercial medical and industrial scanners use this type of X-ray source. In contrast, synchrotron radiation is electromagnetic radiation emitted by high-speed electrons spiraling in a magnetic field of a particle accelerator. The electron beam is steered and focused in a ring by large electromagnets, resulting in the

emission of synchrotron radiation by the decelerating electrons. Depending on the electron's energy and the strength of the magnetic field, the electromagnetic spectrum can consist of microwaves, radio waves, infrared light, visible light, or X-rays. Thus, synchrotron sources also produce polychromatic (white) radiation, however it is of such a high intensity that it can be made monochromatic (single energy) and still have a sufficient photon flux for tomographic (and many other) applications. The reader is referred to McCullough (1975) for a more detailed description of how X-rays (photons) interact with solid matter.

A beam of X-rays is characterized by its photon flux density or intensity and spectral energy distribution. When a beam of X-rays passes through homogeneous material, the object itself becomes a source of secondary X-rays and electrons. Because of these secondary processes, a portion of the primary beam is absorbed or scattered out of the beam. For monochromatic radiation with an incident intensity I_0, the X-ray beam is attenuated after passing through a sample of thickness $D[L]$, to yield an attenuated intensity I, with a magnitude described by Lambert–Beer's law

$$I = I_0 \exp(-\mu D) \tag{1}$$

where μ is the sample-representative linear attenuation coefficient $[L^{-1}]$, which depends on the electron density of the material, the energy of the radiation, and the bulk density of the sample material. Despite the fact that both industrial and medical X-ray sources emit polychromatic X-rays consisting of a spectrum of different wavelengths, which are subject to preferential absorption of the lower energy photons, application of the X-ray technique generally assumes that attenuation is governed by Eq. (1). As will be discussed later, the preferential adsorption of the low energy photons of the polychromatic beam causes artifacts. For a medium consisting of solid, gas, and water phases, Eq. (1) can be written as

$$I = I_0 \exp(-[(1 - \phi)\mu_s \rho_s D + \phi S_w \mu_w \rho_w D]) \tag{2}$$

where the subscripts s and w denote solid and water, ρ the object density $[ML^{-3}]$, Φ the porosity and S_w is the water saturation. This formulation assumes that attenuation by the gaseous air phase is negligible. This may not be the case when working with high vapor pressure liquids. The linear attenuation coefficients for the various object components are obtained by multiplying mass attenuation coefficients $[L^2M^{-1}]$ by mass density $[ML^{-3}]$. The mass attenuation coefficients, in turn, can be obtained from tables (Saloman et al., 1988) or from the NIST XCOM database web site accessible at http://physics.nist.gov/PhysRefData/Xcom/Text/XCOM.html.

In contrast to the two-dimensional representation obtained by radiography, the computed axial tomography (CAT or CT) technique was developed in the medical sciences in the late sixties and early seventies by Hounsfield (1973) to determine the spatial distribution of attenuation values within the object from multiple ray measurements. CT required the development of mathematical reconstruction techniques capable of inversely solving a modified version of Eq. (1), allowing for the estimation of the spatial variation of attenuation values along the ray path

$$I = I_0 \, e^{-\int_D \mu(x)\mathrm{d}x} \tag{3}$$

In this equation, the attenuation of each individual voxel is determined by the phase composition within each voxel.

The transmitted radiation data are analyzed by a computer-intensive reconstruction algorithm to produce a three-dimensional map of linear attenuation values for the object. Since then, the technique has seen extensive use outside the medical field and increasingly sophisticated reconstruction algorithms have been developed to increase accuracy, spatial resolution, and decrease computation time (Flannery et al., 1987).

There are two methods in general use for detection of X-rays. The first method relies on the transmitted X-rays to produce a photochemical change in a photographic emulsion. A second approach is based on the ability of X-rays to either ionize gases or solids, or to produce fluorescence in a crystal. These electronic detectors are the ones used most commonly in tomographic applications. Increasingly more capable detectors have been developed and among the more recent devices is the linear diode array detector for which the X-ray attenuation across the full width of the scanned object is measured by an array of detectors, see Fig. 1(a). Further improvement was accomplished by introduction of the charge-coupled device (CCD)
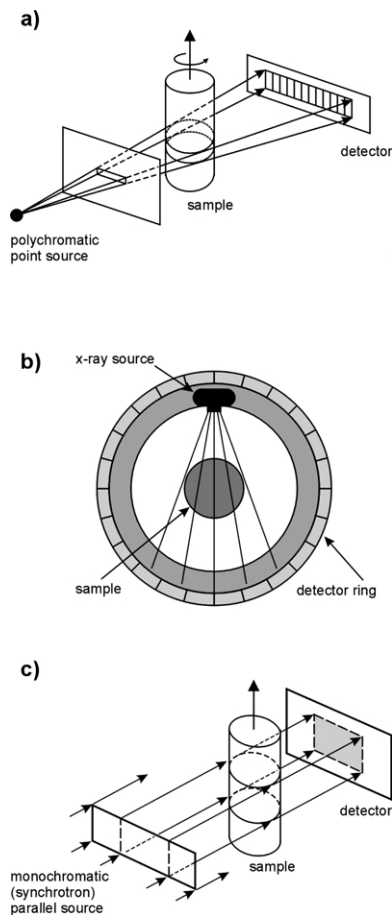
Fig. 1. The tomography setup for the three different systems used: (a) LCAT industrial system, (b) commercial medical system, and (c) GSECARS synchrotron-based microtomography facility. Both (a) and (b) rely on polychromatic X-ray sources, whereas in (c) the source is (white) synchrotron light which is decomposed to a specific (monochromatic) energy level, see Kinney and Nichols (1992) for details.

detector, which provides an areal arrangement of diodes, thereby allowing for simultaneous attenuation measurements of multiple stacked planes, producing an instantaneous three-dimensional map of attenuation values (Fig. 1(c)). Since the CCD measures visible light intensity, it is used with a high-resolution scintillator (e.g. Yttrium–Aluminum–Garnet phosphor screen) that converts X-rays into visible light. Imaging optics may be used to increase the spatial resolution of the CCD detector. The reader is referred

to Stock (1999) and Ketcham and Carlson (2001) for further details of different tomography techniques.

3. Limitations and error sources

3.1. Artifacts

For polychromatic beams, the low energy and thus strongly attenuated photons are eliminated from the beam at a faster rate than the higher, weakly attenuated energy levels. Consequently, the longer the ray paths through the object, the more low energy photons are absorbed, resulting in a more penetrating beam. This phenomenon is called beam hardening, and creates an apparent higher attenuation near the periphery of an otherwise homogeneous sample material. Beam-hardening artifacts can be reduced (Ketcham and Carlson, 2001) by (1) pre-hardening the beam using an attenuating filter (aluminum, copper or brass), (2) using smaller samples, (3) correction during image reconstruction, or can be entirely avoided by using monochromatic synchrotron radiation. Ring artifacts are caused by local defects in the scintillator or detection device, resulting in faulty low or high beam intensities, which appear as rings in the reconstructed CT image. Also, cosmic or scattered X-rays hitting the detector chip directly can cause anomalously bright pixels (zingers) and result in ring artifacts. A more detailed description of various artifacts and their corrections for polychromatic radiation are discussed in Clausnitzer and Hopmans (2000), and in Rivers et al. (1999) or http://www-fp.mcs.anl.gov/xray-cmt/rivers/tutorial.html for monochromatic (synchrotron) radiation.

3.2. Spatial resolution

Spatial resolution describes the level by which details in an image can be resolved. It is generally quantified as the smallest separation distance for which attenuation values at two known points can be perceived as separate entities and thereby accurately measured. The spatial resolution of CT images is determined by size and type of X-ray source and detector, distance between source, object, and detector, potential use of imaging optics, and signal-to-noise ratio, e.g. Stock (1999). According to Kinney

and Nichols (1992), high spatial resolution also depends on the ability to collimate the source, since source divergence leads to image blur. Because source collimation reduces X-ray intensity, the problems of spatial resolution and contrast sensitivity are interrelated. Moreover, the time required to image a volume element or voxel with a certain statistical confidence increases drastically as the size of the voxel decreases. An object of smaller cross-section will absorb fewer photons and therefore requires longer exposure time to assure acceptable counting statistics. Consequently, increasing spatial resolutions require larger incident photon intensity or longer integration times. Because tube X-ray sources emit only a small fraction of their dissipated power as X-rays, obtaining high spatial resolution with these types of sources is often obtained at the cost of counting statistics and the ability to distinguish more subtle low-contrast features in an object. Synchrotron-based radiation on the other hand is well suited for high-resolution imaging because of the extremely high photon flux available. However, because it is difficult to produce energies above approximately 50 keV with synchrotron radiation sources, maximum sample size is generally limited to a few centimeters to assure that the beam can penetrate the sample, whereas larger samples can be examined in conventional systems that generally use higher energies. As a common rule, one can expect a spatial resolution on the order of 200–500 μm for medical CT systems, between 50 and 100 μm for industrial systems (no dose restrictions) designed to examine small samples (Kinney and Nichols, 1992), and from 50 μm down to approximately 1 μm for synchrotron based CT systems. Some of the more recent industrial X-ray systems (e.g. the Skyscan desk-top micro-tomography system used by Van Geet and Swennen (2001)) are capable of spatial resolutions below 10 μm. When a phosphor screen is used to convert X-rays to visible light, its crystal resolution generally becomes the limiting factor with respect to image spatial resolution.

3.3. Contrast sensitivity

Contrast is a measure of how well a feature can be distinguished from the surrounding background. It is often defined by the difference in attenuation between the feature and background, divided by the background attenuation. The ability to discriminate between two materials with closely similar linear attenuation values depends on the accuracy with which the values of μ can be determined (Denison et al., 1997). The linear attenuation coefficient depends on the photon energy of the X-ray beam (E), the electron density of the material (ρ_e), and the effective atomic number of the material (Z) and can be approximated as the sum of Compton scatter and photoelectric contributions:

$$\mu = \rho_e \left(a + \frac{bZ^{3.8}}{E^{3.2}} \right) \tag{4}$$

where a (Klein–Nishina coefficient) is only weakly dependent on energy level, and b is a constant (Vinegar and Wellington, 1987). The electron density is given by (McCullough, 1975)

$$\rho_e = \rho \frac{Z}{A} N_{AV} \tag{5}$$

where ρ is the object density, Z and A the atomic number and atomic weight, and N_{AV} is the Avogadro's number. For low X-ray energies of 50–100 keV, X-rays interact with matter predominantly by photoelectric absorption, which is strongly dependent on atomic number (i.e. by $Z^{3.8}$). For higher energies, up to 5–10 MeV, photon attenuation is largely caused by Compton scattering, and is largely controlled by electron density, whereas for photon energies beyond 10 MeV pair production dominates, e.g. McCullough (1975). Thus, for most practical purposes only the first two mechanisms need to be considered. As is evident from Eq. (4), two materials with different electron densities and atomic compositions can result in similar linear attenuation values, if a difference in electron density of one material is compensated by a similar difference in atomic number of the other material. In this case, dual-energy imaging can provide contrast between two materials using the difference between the effects of Compton scattering and photoelectric absorption. Enhanced contrast can also be achieved by adding a relatively heavy element to, for instance, the fluid phase and adjusting the X-ray energy to levels immediately below and above the photoelectric absorption edge for the element. In this way, high-atomic number salts can be used to enhance contrast in a water phase and analogously

iodated oils for oil phase contrast. We refer to Vinegar and Wellington (1987) for possible choices of such dopants. The dual-energy approach also makes it possible to obtain contrast between two different materials (without using dopants) that would otherwise not be detectable from images produced by single-energy scans.

With respect to both spatial resolution and contrast sensitivity it is important to select an appropriate X-ray source for the material in question. The X-rays need to be sufficiently energetic to penetrate the sample, such that adequate counting statistics can be obtained. On the other hand, if the source is too powerful, the relative attenuation will be low and the object becomes virtually transparent, with little or no contrast between the various phases.

4. The three X-ray systems

4.1. Industrial tube X-ray (Lawrence Livermore National Laboratory, LCAT)

The Linear Computed Axial Tomography (LCAT) setup of the Non-destructive Evaluation Section at Lawrence Livermore National Laboratory is based on a Comet 160 keV X-ray tube with a 0.2 mm focal spot (Roberson et al., 1994). It is a rotate-only system (see Stock (1999) for details on the different generations of scanners) that employs a solid-state linear array detector with gadolinium oxisulfide coated photodiodes. A 0.4 mm Cu-filter is used to minimize beam-hardening effects. Objects to be inspected in the LCAT scanner are rotated in a fan-beam of radiation at constant velocity, see Fig. 1(a). The use of the linear array detector means that each scan produces one (two-dimensional) slice of the inspected object of approximately 0.4 mm thickness. The sample is translated vertically and multiple scans are combined to establish a three-dimensional image. Reconstruction of the data was done with a convolution back-projection algorithm (Roberson et al., 1994).

4.2. Medical scanner (Siemens Somatom Plus S)

The medical scanner of the Center for Phase Equilibria and Separation Processes at the Technical University of Denmark is a commercially available fourth-generation scanner, with resolution between 100 and 500 μm. In principle, the system is similar to the LCAT system, except that the source and detector rotate around the object as shown in Fig. 1(b), and that the energy range is from 85 to 130 keV. As for the LCAT system, one horizontal slice (of 1 or 2 mm thickness) is acquired for each scan/rotation and multiple scans must be combined to obtain a volumetric image. The data are reconstructed with proprietary software provided by Siemens™.

4.3. Synchrotron X-ray system (advanced photon source)

The GeoSoilEnviroCARS (GSECARS) bending magnet beam-line 13-BM-D (sector 13 at the Advanced Photon Source (APS) at Argonne National Laboratory) provides a fan beam of high-brilliance radiation, which is collimated to a parallel beam with a vertical size of about 5 mm. When used with a monochromator (channel-cut Si), energies in the range from 8 to 45 keV can be obtained with a beam size of 50 mm width and 5 mm height (Rivers et al., 1999). Using a monochromator, the white synchrotron light is decomposed into different wavelengths, so that it is possible to customize the radiation to the desired monochromatic energy level. As mentioned earlier, this makes it possible to enhance the contrast between different phases by scanning at the peak absorption energy of an added chemical dopant. The stage setup is similar to the LCAT system as the object can be translated and rotated automatically in the beam, however since the detector is two-dimensional, a complete three-dimensional image is obtained in each scan/rotation, Fig. 1(c). The transmitted X-rays are converted to visible light with a synthetic garnet (YAG) scintillator. The visible light from the scintillator is imaged with a 5 × Mitutoyo microscope objective onto a high-speed 12-bit CCD camera (Princeton Instruments Pentamax), with 1317 × 1035 pixels, each $6.7 \times 6.7 \ \mu m^2$ in size. The raw data used for tomographic reconstruction are 12-bit images and a total of 360 such images were collected as the sample was rotated twice from 0 to 180° in 0.5° steps. Reconstruction was done with filtered back-projection using the programming language IDL™ (Research Systems Inc.).

5. Results and discussion

All samples used for quantitative comparison in this work consisted of fine sand (Lincoln), except for a slightly coarser material (RMC Lone Star, #30) that was used for the APS_27 sample. The mean particle sizes for the fine and coarse sands were 0.17 and 0.45 mm, respectively. All samples were packed in concentric Lucite™ holders with diameters and spatial resolutions as listed in Table 1. Porous membranes separated air and water phases during drainage in all sample holders, and the sample outlet end was connected hydraulically to a drainage reservoir where the drained amount of water was measured. Example images, shown from left to right according to decreasing sample size in Fig. 2, shows the resolution and detail of the different images. Two images for identical spatial locations are presented for each sample, one close to full saturation and the other for samples that were drained to a capillary pressure of approximately 70 cm. In Fig. 2, each pair of images have been scaled to the same minimum and maximum grayscale and also set to the same threshold to allow quantitative comparison of the wet and dry images. In Table 1, the 'energy' level refers to the maximum energy of the photons produced for the tube systems (thus also including photons with much lower energy), whereas for the synchrotron system it is the particular monochromatic energy chosen, and it should be kept in mind that the two are therefore not entirely comparable.

The samples were drained by either applying air pressure or by water suction, i.e. by lowering the drainage reservoir to the desired level relative to the sample. In the two high-resolution images in Fig. 2(d) and (e) (APS_6 and APS_1.5) the samples were saturated with a 13% (weight) solution of KI, whereas sample IVC-SEP (Fig. 2(b)) was saturated with a 5% (weight) solution of KI to enhance contrast. In the high-resolution images in Fig. 2 (and all subsequent images), white/light gray represents the water phase (high attenuation), black is the air phase, and the darker gray is the solid phase. In Fig. 2(a)–(c) this definition is not entirely justifiable because each pixel is likely to contain more than one phase, and also because the liquid phase in Fig. 2(a) and (c) contain no dopant. Therefore, in these images the lighter shades represent higher macroscopic saturation, whereas the

Table 1
Sample size and resolution for the different X-ray systems

Instrument	Energy (keV)	Sample diameter (mm)	Voxel size (μm)
LCAT	160	76	$368 \times 368 \times 368$
IVC-SEP	120	76	$150 \times 150 \times 2000$
APS_27	50	27	$76 \times 76 \times 76$
APS_6	33.7	6	$17 \times 17 \times 17$
APS_1.5	33.7	1.5	$6.7 \times 6.7 \times 6.7$

darker areas represent drier areas (instead of representing individual phases). The lower resolution images provide macroscopic information about the variation in saturation for the bulk sample, as characterized by differences in linear attenuation. In the images of both the industrial (Fig. 2(a)) and medical systems (Fig. 2(b)) it is possible to detect heterogeneous drainage patterns in the samples, but pore-space features cannot be detected. In contrast, the synchrotron images provide information about pore space geometry, but may have poor phase contrast, without adding a chemical dopant to the water phase. For example, in Fig. 1(c), it is difficult to detect differences between the saturated and drained image for the APS_27 images. The synchrotron X-rays are relatively soft (low energy), and attenuation is therefore dominated by photoelectric absorption. Without addition of the iodine, the difference in atomic weight is not sufficient to provide satisfactory contrast between the phases. Above 100 keV, as is the case for the LCAT and IVC-SEP systems, the attenuation is mostly due to Compton scatter which is mainly dependent on electron density. This makes it possible to obtain better phase contrast with the higher energy systems without absorption-edge attenuation. In the past we have obtained similar contrast to that shown in Fig. 2(b) with the medical system (IVC-SEP) without the addition of KI to the water phase. Once KI is added to the water phase and the monochromatic energy adjusted to a level slightly higher than the absorption edge for iodine (33.7 keV), the improvement is clear for the synchrotron system (APS_6 and APS_1.5). The three phases can now be resolved (partly also due to better resolution in the smaller samples) and pore scale processes may be readily observed. For ease of illustration, we are only discussing two-dimensional images in this
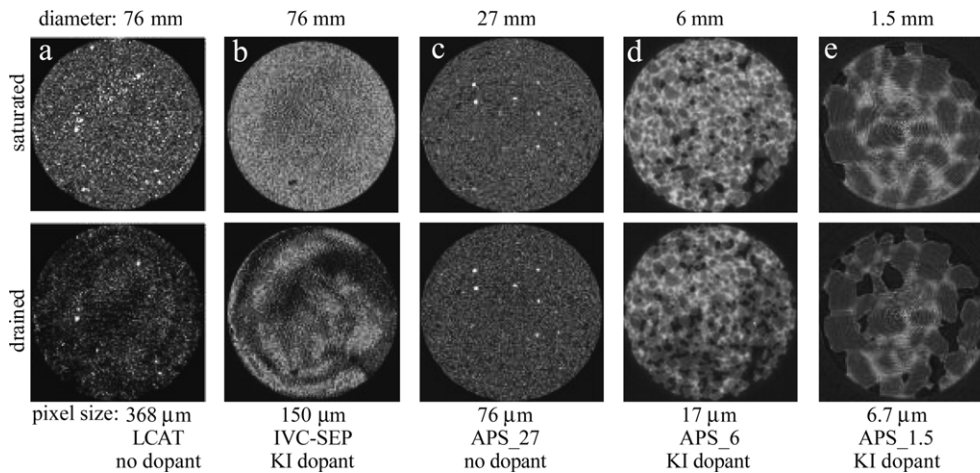
Fig. 2. Horizontal slices through the different samples. In the top row the samples are close to fully saturated and in the bottom row drained to a capillary pressure of approximately 70 cm. In the high-resolution images Fig. 1(d) and (e) white represents the water phase, black is the air phase and gray is the solid phase. Generally, the lighter the image, the higher the linear attenuation coefficient and thus fluid saturation.

publication, however, volumetric information can easily be obtained with tomography, especially when using an areal detector like the CCD detector. As an example, Fig. 3 shows the volumetric detail obtained in a synchrotron-based image of a 6 mm diameter sample of coarse sand.

In Fig. 4, plots of linear attenuation coefficient (μ) as a function of sample height for three of the Lincoln sand samples ((a) LCAT, (b) APS_6, and (c) APS_1.5) are shown. For equal bulk density, the linear attenuation coefficient is linearly related to saturation, with an increase in μ corresponding to an increase in water saturation. Each point in these
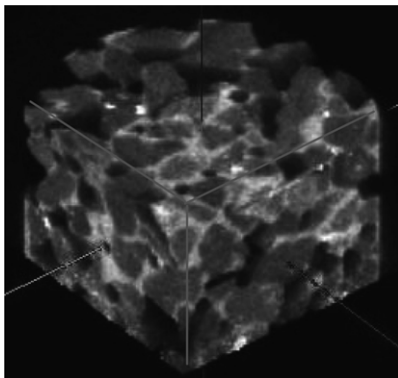

Fig. 3. Example image illustrating the detail of volumetric information obtainable for a 6 mm diameter sample of coarse sand. The very bright white spots are high-density minerals in the sand. Two sides have been cut away to show the sample interior.

profiles is based on the mean linear attenuation coefficient (μ) of a horizontal slice such as those shown in Fig. 2. The LCAT profile (Fig. 4(a)) contains only six points representing scans in six different vertical positions, whereas the APS profiles contain a large number of slices obtained in a single scan by using a CCD detector. Two profiles are shown; corresponding to near saturated and drained conditions, respectively. In accordance with Fig. 2, increasing detail in the profiles can be observed as the sample size is decreased. The slice mean and standard deviation for each profile is listed in Table 2. The noticeable difference in mean linear attenuation coefficient for the LCAT (Fig. 4(a)) and the APS (Fig. 4(b) and (c)) samples are due to the lower energy and the use of iodine and related absorption-edge attenuation in the latter. As seen in Table 2, the standard deviation tends to increase as the spatial resolution increases, but as the mean linear attenuation coefficient also increases, the variation coefficient (VC) remains similar. For the high-resolution images individual grains or pores may occupy many pixels and thus significantly affect the linear attenuation coefficient for the bulk image. Thus, the listed VCs do not necessarily represent a measure of the measurement accuracy. The saturated and drained cases are easily distinguishable for all the samples. For the LCAT sample the difference between saturated and drained condition is 9.4%, whereas for
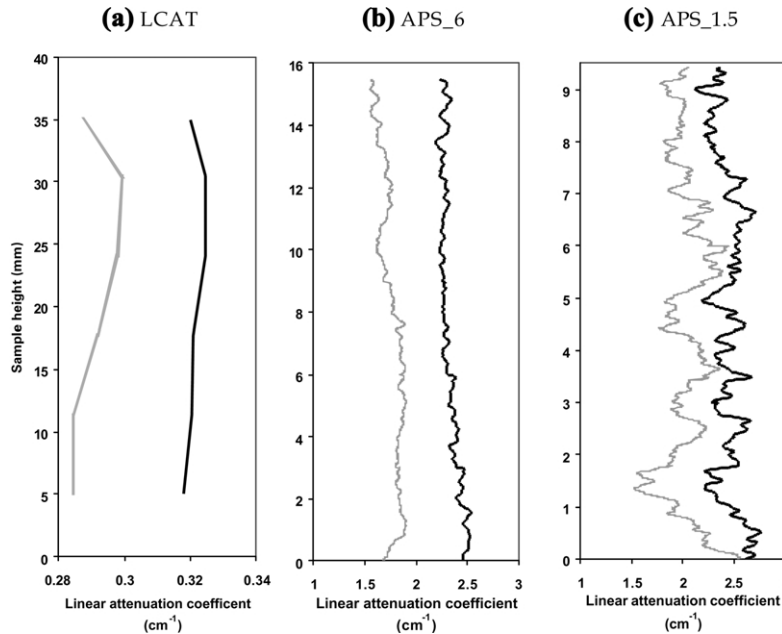
Fig. 4. Profiles of linear attenuation coefficient (μ) for three of the Lincoln sand samples. LCAT (left), APS_6 (center) and APS_1.5 (right). The dark (bold) lines represent saturated conditions and the lighter (thin) lines are drained conditions. The notable difference in μ for the samples is due to use of iodine (and lower energy level) in APS_6 and APS_1.5.

the APS_6 and APS_1.5 samples (using iodine) the differences are 24.5 and 16.8%, respectively. As one would expect, the degree of saturation can be better quantified if the difference in attenuation between saturated and drained conditions is larger.

A measure of the scale dependency of the average linear attenuation is the representative elementary volume (REV) concept, which allows us to treat a porous medium (discontinuous, multi-phase system) as a continuum. It is generally assumed (Bear, 1972) that macroscopic variables (such as average saturation, i.e. linear attenuation coefficient) do not vary with the size of the averaged volume, however, it

Table 2
Statistics of vertical profiles of linear attenuation coefficients in Fig. 4

Instrument		Mean (cm^{-1})	SD (cm^{-1})	VC (%)
LCAT	Saturated	0.32	0.017	5.3
LCAT	Drained	0.29	0.016	5.6
APS_6	Saturated	2.33	0.082	3.5
APS_6	Drained	1.76	0.096	5.5
APS_1.5	Saturated	2.44	0.134	5.5
APS_1.5	Drained	2.03	0.188	9.3

appears from the profile scatter in Fig. 4(c) that the 1.5 mm sample (APS_1.5) might not have a sufficient size to ensure that the averaging volume is large compared to the dimensions of the pore space or individual sand grains. The results of a REV analysis for the APS_6 and APS_1.5 samples are shown in Fig. 5. The linear attenuation coefficient was calculated for a cube of increasing voxel size centered about the center of the volume, with the largest volume defined by a cube that fits inside the diameter of the cylindrical sample. The voxel sizes in Fig. 5 are scaled to the maximum voxel size for a volume to make it possible to effectively compare the two curves. The REV analysis was performed on the samples after they were both drained to approximately residual saturation, and the curves represent average values of scans in three different vertical positions in the sample. Apparently, the APS_6 sample is large enough to adequately represent the attenuation, but this is not quite the case for the 1.5 mm sample for which the linear attenuation coefficient fails to reach a completely stable value within the dimensions of the sample.
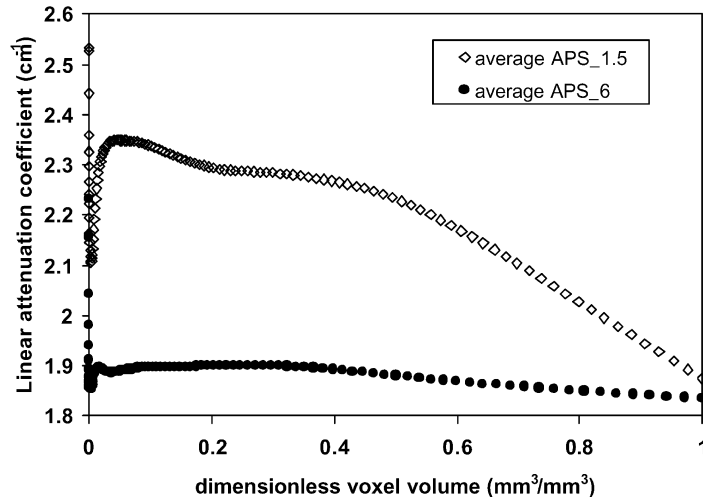
However, for the APS_1.5 image the contrast

Fig. 5. REV analysis for APS_6 and APS_1.5 (both Lincoln sand) showing that the average linear attenuation coefficient for the 6 mm sample reaches a stable value within the sample magnitude, whereas the 1.5 mm sample does not. To compare the two curves, the voxel volumes are plotted as dimensionless voxel volumes, which are scaled by the reciprocal of the maximum volume for the two different sized samples.

and resolution is sufficient to separate all three phases (water, air, and solid). If one is interested in detecting pore scale features such as interfacial contacts, it is also possible to do so by increasing the grain size of the specimen instead of decreasing the specimen size to obtain higher resolution. In Fig. 6, two partially drained images are shown illustrating this effect for a 1.5 mm-diameter sample of fine sand (Fig. 6(a)) and a 6 mm diameter sample of coarse sand (Fig. 6(b)). Similar features can be resolved in the two images, but the larger sample in Fig. 6(b) has much better signal-to-noise ratio because of a larger photon flux through the larger sample, and a more representative REV. In addition, faulty detector pixels or scratches on the scintillator (causing ring artifacts) will be less obvious at the lower magnification or spatial resolution.

For such pore-scale resolution images, as shown for a 6 mm diameter sample of coarse material in Fig. 7(a), it is possible to use image processing techniques (filtering techniques, *k*-means cluster analysis, etc.) or fitting procedures (Clausnitzer and Hopmans, 1999) to partition the phases in their respective volume fractions, as done in Fig. 7(b). Clausnitzer and Hopmans (1999) detail the problems of partial volume effects and present an approach for accurately determining the volume fraction of each phase within

a voxel based on histogram segmentation. Using the cluster analysis approach for the example in Fig. 7 we estimated a porosity of 43.1 (24.1% water and 19.0% air) and thus a water saturation of 55.9%. The phase-segmented image provides quantitative information on porosity, degree and distribution of water (liquid) saturation, as well as the possibility of estimating the interfacial curvature (Fig. 7(c)), and surface area using more advanced image processing techniques, (e.g. medial axis analysis, Brzoska et al., 1999; Coléou et al., 2001).

Differences between drying and wetting branch saturation can also be evaluated in these high-resolution images. In Fig. 8 we show two slices of identical position at identical sample-average saturations, but (a) is obtained during drying, while (b) represents the wetting situation. At this resolution (17 μm per pixel) it is possible to detect pore-scale features like pendular rings between sand grains, and also to observe differences in local saturation between drainage and wetting of the soil sample. Regardless of sample size and resolution it is important to ensure that the experiment is of a sufficient scale to produce results that are representative of the physical processes being investigated, and we provide some recommendations to this point in the following.
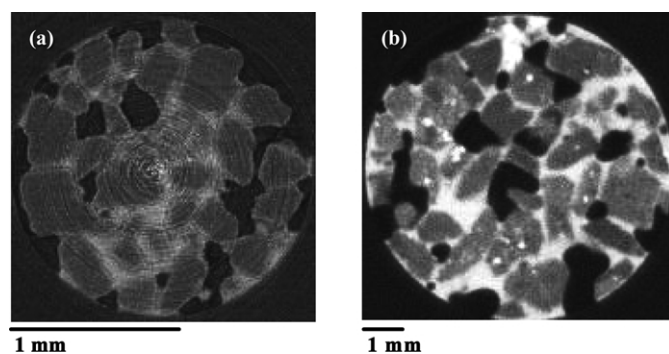
Fig. 6. (a) Fine sand (Lincoln, $d_{50} = 0.17$ mm), 1.5 mm diameter sample, pixel size = 6.7 μm. (b) Coarse sand (8/20, $d_{50} = 0.58$ mm), 6 mm diameter sample, pixel size = 17.1 μm. Similar features can be resolved, but the larger sample has much improved signal-to-noise ratio because of larger photon flux.

6. Recommendations for future work

The choice of CT system as well as specimen size and resulting resolution should be based on the objective of the investigation. If the scope is to investigate specific macroscopic features that are continuous on the scale of the sample, such as macro-pores and cracks, an industrial or medical system may be the preferred choice. These systems work well for investigating non-ideal flow and transport effects like those associated with macro-pores (Perret et al., 1999) and roots (Heeraman et al., 1997; Moran et al., 2000), fractures (Pyrak-Nolte et al., 1997), unstable finger flow, and with flow phenomena such as gas phase entrapment and pore water blockage. Also, if the

focus is variation in saturation over a sample profile or examining boundary effects, the medical systems are advantageous because numerous scans can be obtained over a relatively short period of time, and larger samples can be imaged. Access to medical scanners is also easier than to synchrotron radiation facilities. In general, beam-time at synchrotron facilities is limited to a few days, and experiments must therefore be designed to fit within such a timeframe. It is often easier to get access to a medical scanner over longer periods of time, which means that slow experiments can be performed without compromising boundary condition or equilibration time. However, if the research objective is to identify microscopic pore-scale processes and resolving individual phases, a
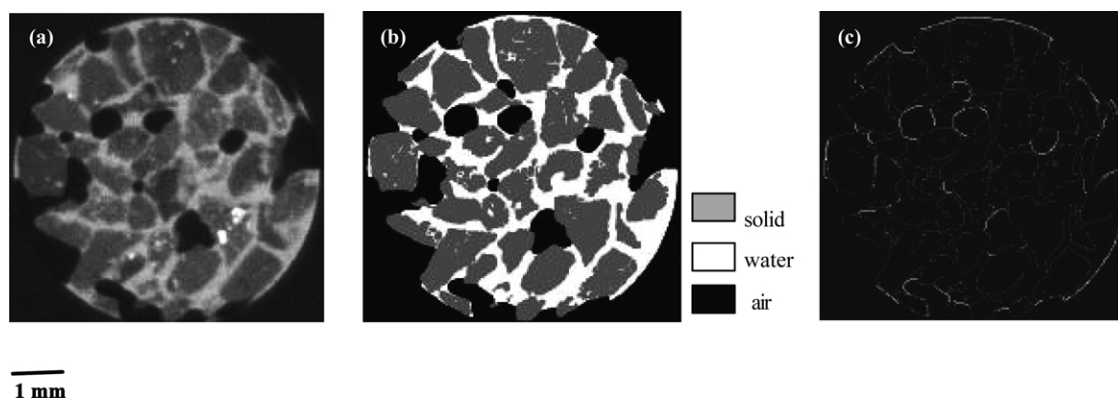

Fig. 7. (a) High-resolution image (APS_6) of a coarse sand ($d_{50} = 0.58$ mm) providing enough detail and contrast to perform a cluster-type image analysis to segment out the three phases illustrated in (b). (b) Solid phase = 56.9%, water phase = 24.1%, and air phase = 19.0% out of a total of 106,272 pixels. The resulting porosity is 43.1% and the water saturation is 55.9%. (c) Air–water interfacial contacts (solid white lines) and solid phase outline (dashed white lines) determined from the segmented image in (b).
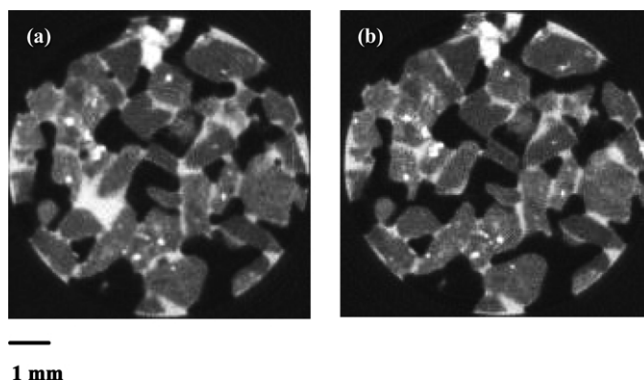
1 mm

Fig. 8. (a) Same slice as Fig. 6(b), but the sample has been drained further to establish pendular rings, which are clearly visible between individual sand grains. (b) Same slice as (a), but now on the wetting curve. The sample has the same average saturation, but local saturation differs distinctly.

synchrotron or a high-resolution industrial X-ray source is required. A disadvantage of the high-resolution systems is, as previously mentioned, the limited specimen size. With respect to data handling, a weakness of the medical systems is that the reconstruction software generally is proprietary, whereas raw data are available for processing with alternative and flexible reconstruction algorithms when using industrial and synchrotron systems.

In the future we expect that advances in beam-line instrumentation at GSECARS will make it possible to significantly reduce the time required for a full rotation/scan, generating opportunities for performing dynamic flow and transport experiments. The ability to obtain such information will be of major importance for verification of new developments both with respect to theory as well as numerical modeling of pore-scale processes. Also, as the experimental techniques and image analysis tools for processing interfacial contact information improve, it might be possible to track mass transfer rates across phase interfaces.

Acknowledgments

References

Anderson, S.H., Peyton, R.L., Gantzer, C.J., 1990. Evaluation of constructed and natural soil macropores using X-ray computed tomography. Geoderma 46, 13–29.

Auzerais, F.M., Dunsmuir, J., Ferreol, B.B., Martys, N., Olson, J., Ramakrishnan, T.S., Rothman, D.H., Schwartz, L.M., 1996. Transport in sandstone: a study based on three dimensional microtomography. Geophys. Res. Lett. 23 (7), 705–708.

Bear, J., 1972. Dynamics of Fluids in Porous Media, Dover Publications, New York.

Brzoska, J.B., Lesaffre, B., Coléou, C., Xu, K., Pieritz, R.A., 1999. Computation of 3D curvatures on a wet snow sample. Eur. Phys. J. Appl. Phys. 7, 45–57.

Celia, M.A., Reeves, P.C., Ferrand, L.A., 1995. Recent advances in pore scale models for multi-phase flow in porous media. Rev. Geophys. 33, 1049–1057.

Clausnitzer, V., Hopmans, J.W., 1999. Determination of phase-volume fractions from tomographic measurements in two-phase systems. Adv. Water Resour. 22, 577–584.

Clausnitzer, V., Hopmans, J.W., 2000. Pore-scale measurements of solute breakthrough using microfocus X-ray tomography. Water Resour. Res. 36 (8), 2067–2079.

Coles, M.E., Hazlett, R.D., Muegge, E.L., Jones, K.W., Andrews, B., Dowd, B., Siddons, P., Peskin, A., Spanne, P., Soll, W.E., 1998. Developments in synchrotron X-ray microtomography

with applications to flow in porous media. SPE Reservoir Eval. Engng August, 288–296.

Coléou, C., Lesaffre, B., Brzoska, J.B., Ludwig, W., Boller, E., 2001. Three-dimensional snow images by X-ray microtomography. Ann Glaciol. 32, 75–81.

Denison, C., Carlson, W.D., Ketcham, R.A., 1997. Three-dimensional quantitative textural analysis of metamorphic rocks using high-resolution computed X-ray tomography: part I. Methods and techniques. J. Metamorphic Geol. 15, 29–44.

Ferreol, B., Rothman, D.H., 1995. Lattice-Boltzmann simulations of flow through Fontainebleau sandstone. Transport Porous Media 20, 3–20.

Flannery, B.P., Deckman, H.W., Roberge, W.G., D'Amico, K.L., 1987. Three-dimensional X-ray micro-tomography. Science 237, 1439–1444.

Hassanizadeh, S.M., Gray, W.G., 1993. Thermodynamic basis of capillary pressure in porous media. Water Resour. Res. 29, 3389–3405.

Hazlett, R.D., 1995. Simulation of capillary-dominated displacements in microtomographic images of reservoir rocks. Transport Porous Media 20, 21–35.

Heeraman, D.A., Hopmans, J.W., Clausnitzer, V., 1997. Three dimensional imaging of plant roots in situ with X-ray computed tomography. Plant Soil 189 (2), 167–179.

Held, R.J., Celia, M.A., 2001. Modeling support of functional relationships between capillary pressure, saturation, interfacial area and common lines. Adv. Water Resour. 24, 325–343.

Hopmans, J.W., Vogel, T., Koblik, P.D., 1992. X-ray tomography of soil water distribution in one-step outflow experiments. Soil Sci. Soc. Am. J. 56 (2), 355–362.

Hounsfield, G.N., 1973. Computed transverse axial scanning (tomography). I. Description of system. Br. J. Radiol. 46, 1016.

Ketcham, R.A., Carlson, W.D., 2001. Acquisition, optimisation and interpretation of X-ray computed tomographic imagery: applications to the geosciences. Comput. Geosci. 27, 381–400.

Kinney, J.H., Nichols, M.C., 1992. X-ray tomographic microscopy (XTM) using synchrotron radiation. Annu. Rev. Mater. Sci. 22, 121–152.

McCullough, E.C., 1975. Photon attenuation in computed tomography. Med. Phys. 2, 307–320.

Moran, C.J., Pierret, A., Stevenson, A.W., 2000. X-ray absorption and phase contrast imaging to study the interplay between plant roots and soil structure. Plant Soil 223 (1–2), 99–115.

Perret, J., Prasher, S.O., Kantzas, A., 1999. Three-dimensional quantification of macropore networks in undisturbed soil cores. Soil Sci. Soc. Am. J. 63 (6), 1530–1543.

Petrovic, A.M., Siebert, J.E., Rieke, P.E., 1982. Soil bulk density analysis in three dimensions by computed tomography scanning. Soil Sci. Soc. Am. J. 46, 445–450.

Pyrak-Nolte, L.J., Montemagno, C.D., Nolte, D.D., 1997. Volumetric imaging of aperture distributions in connected fracture networks. Geophys. Res. Lett. 24 (18), 2343–2347.

Rivers, M.L., Sutton, S.R., Eng, P., 1999. Geoscience applications of X-ray computed microtomography. Proceedings of the SPIE Conference on Developments in X-ray Tomography II, Denver, CO, July 1999, pp. 78–86.

Roberson, G.P., Ryon, R.W., Bull, N.L., 1994. Characterization of mixed waste for sorting and inspection using non-intrusive methods. Lawrence Livermore National Laboratory UCRL-ID-119298.

Saloman, E.B., Hubbell, J.H., Scofield, J.H., 1988. X-ray attenuation cross sections for energies 100 eV to 100 keV and elements $Z = 1$ to $Z = 92$ atomic data and nucleus data tables, p. 38.

Stock, S.R., 1999. X-ray microtomography of materials. Int. Mater. Rev. 44, 141–164.

Van Geet, M., Swennen, R., 2001. Quantitative 3D-fracture analysis by means of microfocus X-ray computer tomography (μCT): an example from coal. Geophys. Res. Lett. 28 (17), 3333–3336.

Vinegar, H.J., Wellington, S.L., 1987. Tomographic imaging of three-phase flow experiments. Rev. Sci. Instrum. 58 (1), 96–107.